

Supporting Information

Yoo et al. 10.1073/pnas.0913879107

SI Text

Titration Experiments. Ideally, we would measure the ionization constants at 100 °C, the temperature at which dichloroacetic acid (DCA) treatment is carried out because ionization constants are known to vary with temperature (1). Because water evaporation can affect the concentration of the solutions during a single titration experiment, we opted to conduct our titration experiments at 70 °C to eliminate the possibility of water loss. The pK_a of the acids is given by the pH at the half point to neutralization (1). Fig. S1 shows the titration curves of (A) DCA, (B) poly(2-acrylamido-2-methyl-1-propanesulfonic acid) (PAAMPSA), and (C) poly(styrene sulfonic acid) (PSS). The pK_a s of DCA, PAAMPSA, and PSS are 0.70, 2.29, and 1.95, respectively, at 70 °C. For comparison, we also determined the pK_a s of these acids at room temperature. The pK_a s of DCA, PAAMPSA, and PSS are 1.21, 2.41, and 2.10, respectively, and those of DCA (2) and PSS (3) are in accordance with values reported elsewhere.

Variable Temperature Conductivity Measurements on PANI-PAAMPSA.

We conducted variable temperature conductivity measurements in a cryostat from 81 to 298 K on untreated and DCA-treated PANI-PAAMPSA to examine the nature of charge transport. Fig. S2A shows the temperature-dependence of the conductivity of untreated poly(2-acrylamido-2-methyl-1-propanesulfonic acid) (PANI-PAAMPSA). We carried out two-point probe measurements on untreated PANI-PAAMPSA because its conductivity at low temperatures was too low to be analyzed by four-point probe setup. Because the bulk resistance of PANI-PAAMPSA is high, we assumed that the contact resistance is negligible. Below 130 K, the bulk resistance of PANI-PAAMPSA exceeds the instrument limitation so we were not able to acquire data beyond this point. The conductivity measured using the cryostat setup is an order of magnitude lower than that measured in air. The reduction in conductivity of PANI-PAAMPSA in the cryostat is attributed to the absence of water, which reduces macroscopic conduction in PANI via proton transfer (4). Although the use of the two-probe setup and water loss during measurement affect the absolute magnitude of the conductivity of PANI-PAAMPSA, they do not affect the temperature-dependence of the conductivity measured. Fig. S2A shows that the conductivity of PANI-PAAMPSA decreases from 10^{-2} S/cm at room temperature in the cryostat to 10^{-6} S/cm at 130 K. This exponential dependence on temperature is consistent with quasi-one-dimensional hopping of carriers (5–8), and is quantitatively described in Eq. S1. This observation indicates that charge transport in PANI-PAAMPSA is enabled by thermally activated hopping of carriers (5–8).

$$\sigma(T) = \sigma_o \exp \left[- \left(\frac{T_o}{T} \right)^{1/2} \right] \quad [S1]$$

In Eq. S1, σ is the conductivity, σ_o is a proportionality constant, T is the absolute temperature, and T_o is a measure of the barrier to charge transport in units of temperature (5–8). Fitting the data in Fig. S2A to Eq. S1 reveals $T_o = 19,980$ K for untreated PANI-PAAMPSA. Fig. S2B shows the temperature dependence of the conductivity of DCA-treated PANI-PAAMPSA. These measurements were made with a four-point probe method so we were able to precisely remove the contribution of contact resistance. Because the sample was unencapsulated, it also suffers from moisture removal in the cryostat setup. Similar to the temperature-dependence of the conductivity of PANI-PAAMPSA, the conductivity of DCA-treated PANI-PAAMPSA decreases with

decreasing temperature; this temperature dependence is also described by Eq. S1, suggesting that charge transport in DCA-treated PANI-PAAMPSA is also thermally activated. Fitting the data to Eq. S1 yields $T_o = 1,690$ K. That T_o is an order of magnitude smaller for DCA-treated PANI-PAAMPSA compared to untreated PANI-PAAMPSA indicates that hopping is much more efficient in DCA-treated PANI-PAAMPSA compared to untreated PANI-PAAMPSA.

HCl-Treated PANI-PAAMPSA. Fig. S3A and B show representative atomic force micrographs (AFMs) of untreated and HCl-treated PANI-PAAMPSA films, respectively. The AFMs of HCl-treated PANI-PAAMPSA is similar to that of untreated PANI-PAAMPSA; we observe globular structures that are reminiscent of the electrostatically stabilized colloidal particles in both micrographs. The rms roughness of HCl-treated PANI-PAAMPSA film is 58.7 nm (the rms roughness of the untreated film is 60.3 nm). The ultraviolet-visible-near infrared (UV-vis-NIR) spectrum of HCl-treated PANI-PAAMPSA is shown in Fig. S4A, along with those of untreated (Fig. S4B) and DCA-treated (Fig. S4C) PANI-PAAMPSA for comparison. In contrast to the spectrum of DCA-treated PANI-PAAMPSA, the spectrum of HCl-treated PANI-PAAMPSA looks similar to that of pristine PANI-PAAMPSA. A slight red-shift of the polaron transition is observed; this red-shift is associated with the doping of residual imine nitrogens along the backbone of PANI when PANI-PAAMPSA is exposed to HCl (9). Given the preservation of the polaron transition, we believe that HCl-treated PANI-PAAMPSA retains its compact coil conformation; exposure to HCl did not yield significant structural rearrangement.

XPS of PANI-PAAMPSA. Fig. S5A and B show the x-ray photoelectron spectroscopy (XPS) spectra acquired in the nitrogen region of untreated and DCA-treated PANI-PAAMPSA films, respectively. The nitrogen spectrum was deconvoluted into three components (10): the peak located at 399.2 eV is attributed to neutral amine and imine sites in PANI, as well as the amide groups in PAAMPSA; the peak at 400.4 eV is assigned to protonated nitrogens (N_1^+) that are associated with the presence of polarons in PANI-PAAMPSA; the peak located at 401.3 eV is attributed to the protonated nitrogens (N_2^+) that are ionically associated with the sulfonic acid groups of PAAMPSA. A full width at half the maximum intensity (FWHM) of 1.4 eV was maintained during the fitting of all three peaks. Given that the concentration of species present is proportional to the integrated intensity of the relevant peaks, we observe in Fig. S5 that the total concentration of protonated nitrogens (N_1^+ and N_2^+) relative to that of neutral nitrogens changes with DCA treatment. The change in the extent of ionic association between PANI and PAAMPSA is also mirrored in the XPS spectra acquired in the sulfur region of untreated and DCA-treated PANI-PAAMPSA (Fig. S5C and D). The sulfur XPS spectra were deconvoluted into two doublets (7): The doublet with peaks located at 167.5 and 168.7 eV is assigned to the sulfonic acid groups ($-SO_3^-$) of PAAMPSA that are ionically associated with PANI; the other doublet with peaks located at 168.3 and 169.5 eV corresponds to the unionized sulfonic acid groups ($-SO_3H$) of PAAMPSA. The FWHM of the individual peaks of the doublets was kept to 1.0 eV during peak fitting. Consistent with observations in the nitrogen spectra, we observe that the concentration of ionized sulfonic acid groups ($-SO_3^-$) relative to that of unionized sulfonic acid groups ($-SO_3H$) changes with DCA treatment. Our XPS results indicate

that DCA can indeed moderate the strong ionic interactions between PANI and PAAMPSA. DCA—a stronger acid than PAAMPSA—can effectively disrupt the ionic interactions between the sulfonic acid groups in PAAMPSA and the PANI backbone, effectively “dissolving” PANI-PAAMPSA particles whose structures were arrested during template polymerization (11). Exposure to DCA thus allows PANI-PAAMPSA to adopt a structurally more favorable extended chain conformation for charge transport. As a result, the electrical conductivity of PANI-PAAMPSA is improved by more than two orders of magnitude. We do not observe the presence of chlorine during XPS analysis of DCA-treated PANI-PAAMPSA films, indicating an absence of residual DCA. This observation suggests that the conductivity enhancement is not due to DCA doping (12) of PANI.

Conductivity Measurements and Structural Characterization of PANI-PSS. Fig. S6 details the electrical and structural characterization of PANI-PSS films before and after DCA treatment. The representative I - V characteristics of untreated (solid line) and DCA-treated (dashed line) PANI-PSS films are shown in Fig. S6A. The I - V curve of the untreated PANI-PSS film is magnified in the inset. The current is on the order of 10^{-1} mA when a 10 V bias is applied to the untreated PANI-PSS film (solid line). After DCA treatment, the current increases by more than two orders of magnitude at the same applied bias (dashed line). Accordingly, the conductivity increases from 0.17 ± 0.04 S/cm in untreated PANI-PSS films to 42.37 ± 12.49 S/cm in DCA-treated PANI-PSS films. Like DCA-treated PANI-PAAMPSA, this conductivity enhancement is accompanied by drastic structural changes, as indicated by the differences in the UV-vis-NIR spectra in Fig. S6B and the AFMs in Fig. S6C and D. The UV-vis-NIR spectrum of untreated PANI-PSS (solid line) is consistent with that of untreated PANI-PAAMPSA. The broad peak between 310 and 450 nm is attributed to the π - π^* transition of the conjugated PANI backbone, whereas the peak at 800 nm is associated with a polaron interband transition (13–15). The presence of these peaks in the UV-vis-NIR spectrum indicates PANI having a compact coil conformation and is generally associated with PANI having low conductivities (16, 17). After DCA treatment, the polaron interband transition is largely suppressed and a broad absorption appears in the near-IR region. This absorption is generally referred to as the free carrier tail (16, 17) and suggests large extents of delocalization of the charge carriers. The presence of this free carrier tail is associated with PANI having an extended chain conformation (16, 17) that greatly improves charge transport (16, 17). This observation is consistent with changes in the UV-vis-NIR spectrum of PANI-PAAMPSA after DCA treatment. The AFMs of untreated and DCA-treated PANI-PSS in Fig. S6C and D are also consistent with those of untreated and DCA-treated PANI-PAAMPSA. Specifically, the pristine PANI-PSS film surface is rough; an rms roughness of 13.7 nm was extracted from the 5×5 - μm window. Submicron size electrostatically stabilized PANI-PSS particles compose the film. The same film becomes significantly smoother after DCA treatment; the extracted rms roughness is 2.9 nm.

XPS of PANI-PSS. Fig. S7 contains the nitrogen XPS spectra of untreated (Fig. S7A) and DCA-treated (Fig. S7B) PANI-PSS films. We deconvoluted the signal in the nitrogen region using the same procedure outlined for XPS analysis of PANI-PAAMPSA. Given that PAAMPSA is replaced with PSS (no amide groups), the peak at 399.2 eV arises solely from neutral amine and imine in PANI (18). Comparison of the XPS spectra in Fig. S7A and B reveals that the concentration of protonated nitrogens relative to that of neutral nitrogens changes on DCA treatment. This observation is consistent with XPS data analysis carried out in the sulfur region. Specifically, the concentration of ionized sulfonic acid relative to that of unionized sulfonic acid changes with DCA treatment. Just

as in the case of PANI-PAAMPSA, exposure to DCA moderates the ionic interactions between the sulfonic acid groups of PSS and the aniline repeat units. Further, we did not detect the presence of chlorine during the XPS analysis of DCA-treated PANI-PSS films, suggesting the absence of residual DCA in the films. Collectively, our characterization on DCA-treated PANI-PSS indicates that conductivity enhancement in this material is mechanistically comparable to conductivity enhancement in PANI-PAAMPSA; strong acids that are good plasticizers for the polymer acid template can induce structural rearrangement during solvent annealing, leading to enhanced charge transport and a concomitant increase in bulk conductivity.

Conductivity Measurements and Structural Characterization of PEDOT-PSS. Fig. S8 contains the electrical and structural properties of untreated and DCA-treated PEDOT-PSS. The current of untreated PEDOT-PSS film is on the order of 10^{-1} mA at a 10 V bias (Fig. S8A; solid line). The current of the same PEDOT-PSS film increases by more than three orders of magnitude given the same applied voltage after DCA treatment (Fig. S8A; dashed line). This improvement translates to an average conductivity of 0.21 ± 0.05 and 175.39 ± 59.75 S/cm for untreated and DCA-treated PEDOT-PSS films, respectively. Fig. S8B shows the UV-vis-NIR spectra of untreated (solid line) and DCA-treated (dashed line) PEDOT-PSS films. In the UV-vis-NIR spectrum of as-cast PEDOT-PSS film, a peak at 280 nm related to the π - π^* transition and a broad band at approximately 800 nm associated with polaron transition are observed (19, 20). Underlying the polaron interband transition is a continuously increasing background that extends into the near-IR range. This background, attributable to the free carrier tail, suggests that untreated PEDOT-PSS has an extended chain conformation (19, 20). This spectrum is consistent with the UV-vis-NIR spectrum of PEDOT-PSS previously reported (19, 20). After DCA treatment, the UV-vis-NIR spectrum of PEDOT-PSS is comparable to that of pristine PEDOT-PSS; only a slightly stronger absorption in the near-IR region is observed. This observation indicates that DCA treatment of PEDOT-PSS does not induce significant rearrangement of the polymer conformation. Yet, the conductivity of PEDOT-PSS increases significantly after DCA treatment. Fig. S8 shows the AFMs of untreated (Fig. S8C) and DCA-treated (Fig. S8D) PEDOT-PSS films. The untreated PEDOT-PSS film is very smooth with an rms roughness of 0.9 nm over the 5×5 - μm scan window. After DCA treatment, however, the surface of the film roughens. The extracted rms roughness of the DCA-treated PEDOT-PSS film is 2.6 nm. The mechanism by which conductivity improvement occurs in PEDOT-PSS must thus be different from that in PANI-PAAMPSA or PANI-PSS.

XPS of PEDOT-PSS. The XPS spectra of untreated and DCA-treated PEDOT-PSS films in the sulfur region are shown in Fig. S9A and B, respectively. The sulfur spectra were each deconvoluted into three doublets (21). During data fitting, a FWHM of 1.2 eV was maintained for the individual peaks within each doublet. The doublet consisting of peaks at 164.5 and 165.6 eV corresponds to the protonated thiophene units in PEDOT (21). The positive charges in PEDOT are not localized on single monomer units. Rather, they are delocalized over several adjacent rings, resulting in a spread in the binding energies (21, 22). This broad distribution of binding energies results in an asymmetric tail on the higher energy side of the PEDOT sulfur signal (21). The other two doublets, located at higher binding energies compared to the PEDOT sulfur doublet and only separated by 0.4 eV, are associated with the sulfonic acid groups in PSS. The doublet with peaks located at 168.4 and 169.6 eV is attributed to sulfonic acid that is associated with sodium (SO_3Na^+) (21–25). Sodium persulfate ($\text{Na}_2\text{S}_2\text{O}_8$) is frequently used as the oxidizing agent for the synthesis of PEDOT. It has been hypothesized that sodium

ions from residual oxidizing agent can associate with the sulfonic acid groups of PSS (2324). The doublet with peaks located at 168.8 and 170.0 eV is attributed to SO_3H of PSS. Comparing Fig. S9A and B indicates that the sulfur content attributable to PEDOT relative to that attributable to PSS has increased with DCA treatment. This observation suggests that the PEDOT content is enhanced on the surface of the film with exposure to DCA. The oxygen XPS spectra of untreated and DCA-treated PEDOT-PSS films are shown in Fig. S9C and D, respectively. The oxygen spectra were deconvoluted into four different oxygen environments (21). The peak at the highest binding energy (533.7 eV) corresponds to oxygens in the dioxyethylene bridge of PEDOT (21). The peaks located at 532.4 and 533.5 eV correspond to oxygens in the sulfonic acid groups of PSS. Specifically, the peak at the lower binding energy of 532.4 eV originates from oxygens that are double bonded to sulfur in the sulfonic acid groups, whereas the peak at the higher binding energy corresponds to hydroxyl oxygens (21). The peak at 531.9 eV is associated with oxygens in the sulfonic acid groups that are ionically associated with sodium (21). Monitoring the change in the integrated intensity of the peak associated with PEDOT relative to the integrated intensities of the peaks associated with PSS would thus provide a measure of the PEDOT content on the surface of the film. Consistent with differences in the sulfur spectra, a comparison between Fig. S9C and D indicates an enhancement of PEDOT content on the surface of the film after DCA treatment. The suite of structural characterization carried out on pristine and DCA-treated PEDOT-PSS in fact indicates that the mechanism with

which conductivity is enhanced in PEDOT-PSS is fundamentally different from that in PANI-PAAMPSA and PANI-PSS. Solvent annealing PEDOT-PSS appears to selectively disrupt the PSS overlayer (21–25) that is always present when PEDOT-PSS is cast as films. The disruption of this insulating overlayer is in turn responsible for the enhancement in lateral conductivity of PEDOT-PSS.

Organic Solar Cells (OSCs)—Additional Details. Typically, indium tin oxide (ITO) is widely used as the anode in OSCs because of its low resistance and high optical transparency (26). Given the scarcity of indium and its rising costs, there is a strong driving force to find an alternative to ITO for solar cell applications. Here, we assess the use of conducting polymers as replacement candidates for ITO in bulk heterojunction OSCs with a blend of P3HT and PCBM as the active layer. In bulk heterojunction OSCs of P3HT and PCBM, P3HT is responsible for light absorption. Fig. S10 contains the UV-vis-NIR spectra of P3HT (solid black line), untreated (dashed red line) and DCA-treated (dash-dotted blue line) PANI-PAAMPSA, as well as untreated (dotted green line) and DCA-treated (dash-double-dotted black line) PEDOT-PSS. The absorptions of the conducting polymers all occur at higher wavelengths compared to the absorption of P3HT. Given that the absorption ranges of the active layer and the anode are complementary, the incorporation of these conducting polymers as anodes should not significantly influence the light absorption efficiency of active layer.

- Laidler KJ, Meiser JH, Sanctuary BC (2003) *Physical Chemistry*, 4th Ed, ed Stratton E (Houghton Mifflin, Boston), pp. 169–172.
- Lide DR (2006) *Handbook of Chemistry and Physics* (CRC, Boca Raton), p. 42.
- Müller S, et al. (2008) VEGF-functionalized polyelectrolyte multilayers as proangiogenic prosthetic coatings. *Adv Funct Mater* 18:1767–1775.
- Travers JP, Nechtschein M (1987) Water effects in polyaniline: A new conduction process. *Synthetic Met* 21:135–141
- Menon R, Yoon CO, Moses D, Heeger AJ, Cao Y (1993) Transport in polyaniline near the critical regime of the metal-insulator transition. *Phys Rev B* 48:17685–17694.
- Horowitz G (1998) Organic field-effect transistors. *Adv Mater* 10:365–377.
- Kim JY, Jung JH, Lee DE, Joo J (2002) Enhancement of electrical conductivity of poly(3,4-ethylenedioxythiophene)/poly(4-styrenesulfonate) by a change of solvents. *Synthetic Met* 126:311–316.
- Zuppiroli L, Bussac MN, Paschen S, Chauvet O, Forro L (1994) Hopping in disordered conducting polymers. *Phys Rev B* 50:5196–5203.
- Yoo JE, et al. (2007) Improving the electrical conductivity of polymer acid-doped polyaniline by controlling the template molecular weight. *J Mater Chem* 17:1268–1275.
- Yue J, Epstein AJ (1991) XPS study of self-doped conducting polyaniline and parent systems. *Macromolecules* 24:4441–4445.
- Yoo JE, et al. (2009) Polymer conductivity through particle connectivity. *Chem Mater* 21:1948–1954.
- Gmati F, Fattoum A, Bohli N, Dhaoui W, Mohamed AB (2007) Comparative studies of the structure, morphology and electrical conductivity of polyaniline weakly doped with chlorocarboxylic acids. *J Phys—Condens Mat* 19:326203.
- Ginder JM, Epstein AJ (1990) Role of ring torsion angle in polyaniline: Electronic structure and defect states. *Phys Rev B* 41:10674–10685.
- Stafstrom S, et al. (1987) Polaron lattice in highly conducting polyaniline: theoretical and optical studies. *Phys Rev Lett* 59:1464–1467.
- McManus PM, Cushman RJ, Yang SC (1987) Influence of oxidation and protonation on the electrical conductivity of polyaniline. *J Phys Chem* 91:744–747.
- MacDiarmid AG, Epstein AJ (1994) The concept of secondary doping as applied to polyaniline. *Synthetic Met* 65:103–116.
- MacDiarmid AG, Epstein AJ (1995) Secondary doping in polyaniline. *Synthetic Met* 69:85–92.
- Jayanty S, Prasad GK, Sreedhar B, Radhakrishnan TP (2003) Polyelectrolyte templated polyaniline—film morphology and conductivity. *Polymer* 44:7265–7270.
- Ouyang J, Chu C-W, Chen F-C, Xu Q, Yang Y (2005) High-conductivity poly(3,4-ethylenedioxythiophene):poly(styrene sulfonate) film and its application in polymer optoelectronic devices. *Adv Funct Mater* 15:203–208.
- Ouyang J, et al. (2004) On the mechanism of conductivity enhancement in poly(3,4-ethylenedioxythiophene):poly(styrene sulfonate) film through solvent treatment. *Polymer* 45:8443–8450.
- Greczynski G, et al. (2001) Photoelectron spectroscopy of thin films of PEDOT-PSS conjugated polymer blend: A mini-review and some new results. *J Electron Spectrosc* 121:1–17.
- Crispin X, et al. (2003) Conductivity, morphology, interfacial chemistry, and stability of poly(3,4-ethylene dioxythiophene)-poly(styrene sulfonate): A photoelectron spectroscopy study. *J Polym Sci Pol Phys* 41:2561–2583.
- Groenendaal LB, Jonas F, Freitag D, Pielartzik H, Reynolds JR (2000) Poly(3,4-ethylenedioxythiophene) and its derivatives: Past, present, and future. *Adv Mater* 12:481–494.
- Hwang J, Amy F, Kahn A (2006) Spectroscopic study on sputtered PEDOT · PSS: Role of surface PSS layer. *Org Electron* 7:387–396.
- Greczynski G, Kugler T, Salaneck WVR (1999) Characterization of the PEDOT-PSS system by means of x-ray and ultraviolet photoelectron spectroscopy. *Thin Solid Films* 354:129–135.
- Hoppe H, Sariciftci NS (2004) Organic solar cells: An overview. *J Mater Res* 19:1924–1945.

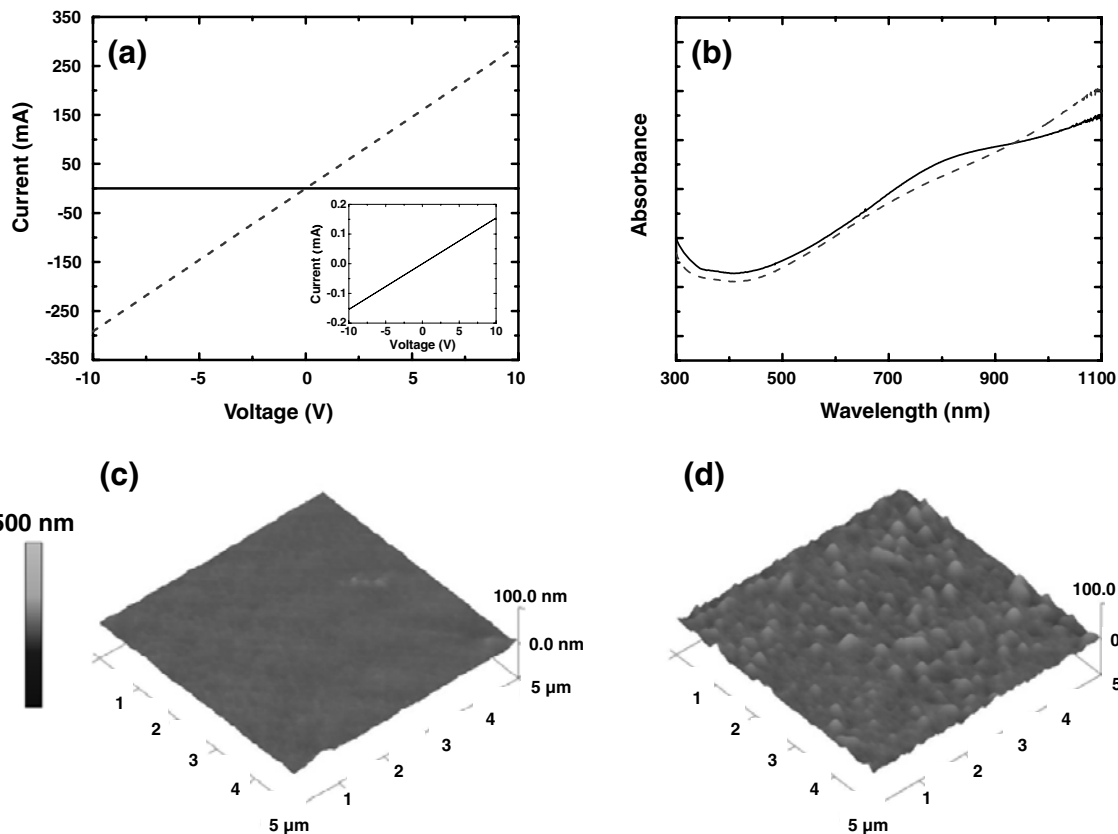


Fig. 58. (A) I - V characteristics and (B) UV-vis-NIR spectra of untreated (solid lines) and DCA-treated (dashed lines) PEDOT-PSS films. Inset of (A): magnified plot of the I - V characteristics of the untreated PEDOT-PSS film. AFM images of (C) untreated (rms roughness of ≈ 0.9 nm) and (D) DCA-treated (rms roughness of ≈ 2.6 nm) PEDOT-PSS films.

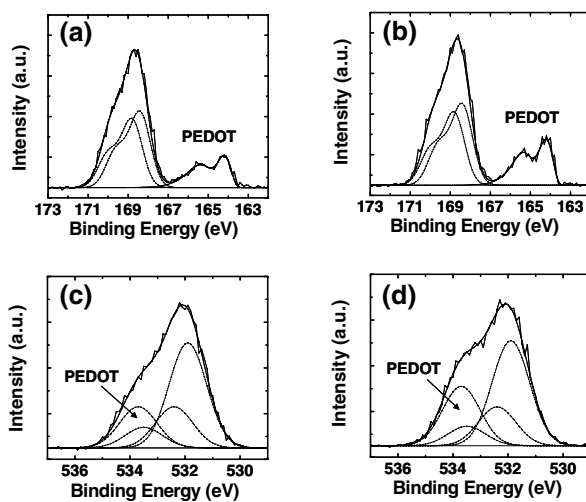


Fig. 59. XPS sulfur spectra of (A) untreated and (B) DCA-treated PEDOT-PSS, and oxygen spectra of (C) untreated and (D) DCA-treated PEDOT-PSS, respectively. Deconvoluted peaks plotted with dotted lines.

